Constriction Rate Modulation Can Drive Cell Size Control and Homeostasis in C. crescentus

iScience

CellPress

Article

Constriction Rate Modulation Can Drive Cell Size Control and Homeostasis in *C. crescentus*

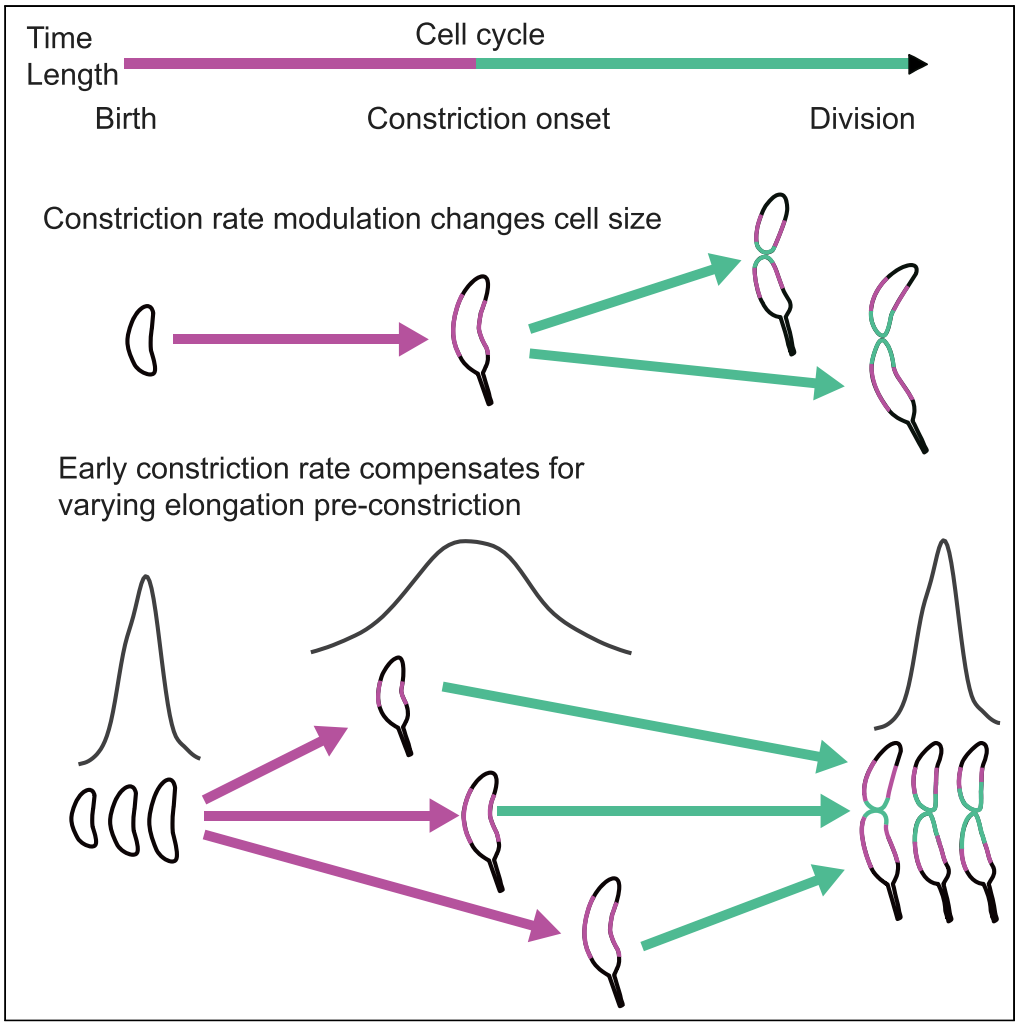

Ambroise Lambert, Aster Vanhecke, Anna Archetti, ..., Michael T. Laub, Erin Goley, Suliana Manley

suliana.manley@epfl.ch

HIGHLIGHTS

Perturbing constriction rate changes cell length

Faster constriction rate results in blunter cell poles

Early constriction rate modulation balances elongation before and during constriction

We propose that constriction rate is set by the accumulation of precursors during elongation

Lambert et al., iScience 4, 180–189
June 29, 2018
https://doi.org/10.1016/j.isci.2018.05.020

iScience

CellPress

Article

Constriction Rate Modulation Can Drive Cell Size Control and Homeostasis in *C. crescentus*

Ambroise Lambert,[1,8] Aster Vanhecke,[1,8] Anna Archetti,[1] Seamus Holden,[1,2] Felix Schaber,[1] Zachary Pincus,[3,4] Michael T. Laub,[5,6] Erin Goley,[7] and Suliana Manley[1,9,*]

SUMMARY

Rod-shaped bacteria typically grow first via sporadic and dispersed elongation along their lateral walls and then via a combination of zonal elongation and constriction at the division site to form the poles of daughter cells. Although constriction comprises up to half of the cell cycle, its impact on cell size control and homeostasis has rarely been considered. To reveal the roles of cell elongation and constriction in bacterial size regulation during cell division, we captured the shape dynamics of *Caulobacter crescentus* with time-lapse structured illumination microscopy and used molecular markers as cell-cycle landmarks. We perturbed the constriction rate using a hyperconstriction mutant or fosfomycin ([(2R,3S)-3-methyloxiran-2-yl]phosphonic acid) inhibition. We report that the constriction rate contributes to both size control and homeostasis, by determining elongation during constriction and by compensating for variation in pre-constriction elongation on a single-cell basis.

INTRODUCTION

Cell size regulation is observed nearly universally among prokaryotes (Koch, 1996), allowing them to both control their size at birth and homeostatically maintain it over multiple generations (Wang et al., 2010). Cell size control and homeostasis are critical for survival: once too small, cells lack the volume required to host the essential machinery of life (National Research Council (US) Steering Group for the Workshop on Size Limits of Very Small Microorganisms 1999) or initiate chromosome segregation (Donachie and Begg, 1989), whereas cells that are too large may suffer limitations in nutrient uptake (Beveridge, 1988) and distribution (Schulz and Jørgensen, 2001) because of their reliance on diffusive transport.

Size regulation is linked to cell cycle progression, which is marked by several key processes, including chromosome replication, segregation, and division into two daughter cells. These processes occur once per cell cycle in bacteria such as *Caulobacter crescentus* (Marczynski, 1999), in contrast to rapidly proliferating organisms such as *Escherichia coli* (Cooper and Helmstetter, 1968) and *Bacillus subtilis*, whose cells often have multi-fork replication and which can, following nutrient up-shifts, initiate replication multiple times in a single cell cycle. In *C. crescentus*, differentiation from a swarmer to a stalked cell and the initiation of chromosome replication and segregation mark the transition from cell cycle phase G1 to S. The completion of replication marks the end of S phase. Once DNA segregation is completed, cells finish cytokinesis to form sibling stalked and swarmer cells during G2/M (Skerker and Laub, 2004).

From the perspective of achieving a given size at birth, "size control," individual *C. crescentus* cells elongate exponentially throughout the cell cycle, as is typical for rod-shaped bacteria. Their growth is divided into an initial stage of dispersed pure elongation as peptidoglycan (PG) is inserted sporadically along the lateral walls, followed by a stage of zonal elongation and then mixed elongation and constriction in G2/M phase during which PG is inserted at mid-cell to build two new poles (Aaron et al., 2007; Kuru et al., 2012). In *B. subtilis*, strains in which the cells are on average longer at the onset of constriction are also on average longer at division (Taheri-Araghi et al., 2015; Weart et al., 2007). This suggests a model for cell size control, by modifying the cell length at which the divisome, the multi-protein complex that guides division, begins to generate constriction. Similarly, in *C. crescentus*, chromosome segregation must initiate before the cytokinetic Z-ring can assemble at mid-cell, coordinated by the gradient-forming FtsZ inhibitor MipZ (Thanbichler and Shapiro, 2006). Another possibility is that the rate of constriction is modulated; this was shown to be the case for MatP, which coordinates chromosome segregation and pole construction in *E. coli* (Coltharp et al., 2016).

[1]Institute of Physics, École Polytechnique Fédérale de Lausanne (EPFL), 1015 Lausanne, Switzerland

[2]Centre for Bacterial Cell Biology, Institute for Cell and Molecular Biosciences, Newcastle University, Newcastle upon Tyne NE2 4AX, UK

[3]Department of Genetics, Washington University in St. Louis, St. Louis, MO 63110, USA

[4]Department of Developmental Biology, Washington University in St. Louis, St. Louis, MO 63110, USA

[5]Department of Biology, Massachusetts Institute of Technology, Cambridge, MA 02139, USA

[6]Howard Hughes Medical Institute, MassachusettsInstitute of Technology, Cambridge, MA 02139, USA

[7]Department of Biological Chemistry, Johns Hopkins University School of Medicine, Baltimore, MD 21205, USA

[8]These authors contributed equally

[9]Lead Contact

*Correspondence: suliana.manley@epfl.ch

https://doi.org/10.1016/j.isci.2018.05.020

For a population to maintain its size over generations, "size homeostasis," different rules have been proposed. In a "sizer" model, cells require a critical size to divide; in an "adder" model, cells add a fixed volume between birth and division; and in a "timer" model, cells maintain the time between divisions. Mixed models that combine aspects of each have had success in capturing a wide range of observations (Banerjee et al., 2017; Osella et al., 2014) and are often justified through their connections with specific cell cycle phases. In *E. coli*, chromosome replication from the start of the cell cycle until S/G2 may have a constant duration, underlying a timer (Cooper and Helmstetter, 1968). The initiation of chromosome replication requires a fixed volume per origin of replication, and a fixed time to divide after initiation. This leads to a sizer under slow growth conditions and a phenomenological adder under fast growth, multi-origin conditions (Ho and Amir, 2015; Wallden et al., 2016). Putative molecular mechanisms have generally relied on the accumulation of proteins above a threshold, such as an "initiator" of unknown identity triggering replication (Sompayrac and Maaløe, 1973) or excess PG cell wall precursors triggering constriction (Harris and Theriot, 2016). A model of the latter case predicts a constant addition of volume per cell cycle, or adder. Indeed, an adder has been observed for *C. crescentus* under a wide range of growth conditions (Campos et al., 2014). Deviations from a pure adder toward a mixed relative timer and adder have also been reported for stalked cells, observed over many generations and a range of different temperatures (Banerjee et al., 2017). Any model incorporating a sizer or adder will allow smaller cells to increase, whereas larger cells to decrease in size over generations until both converge to a size set by the constant of addition (Jun and Taheri-Araghi, 2015). Thus, both provide a clear means for a population to achieve size homeostasis.

Remarkably, although constriction makes up a significant portion of the cell cycle in many bacteria (den Blaauwen et al., 2017), for example, up to 40% for *E. coli* (Reshes et al., 2008) or *C. crescentus* grown in minimal media (Laub et al., 2000), its impact on cell size control and homeostasis has rarely been considered. Intriguingly, budding yeasts may use constriction rate to modulate their size in response to changes in growth conditions (Leitao and Kellogg, 2017). However, a single-cell study of the contribution of the constriction stage in bacteria has been challenging, in part due to the diffraction-limited size of the constriction site and partly due to the need for corroboration by divisome markers to unambiguously identify constriction onset. Furthermore, direct measurement of the instantaneous constriction rate has not been possible.

Here, we investigated whether and how cells adjust their constriction rate to achieve cell size control and homeostasis. We used structured illumination microscopy (SIM) (Gustafsson, 2000) to resolve the constriction site diameter and measure the size of synchronized *C. crescentus* cells as they progressed through their cell cycle. We show that perturbing the constriction rate changes cell size, independent of the elongation rate. Furthermore, we found that within a population the onset of constriction and its rate are coordinated: cells that elongate more than average before constriction undergo a more rapid constriction, leading to less elongation during constriction, and vice versa. This compensation leads to a higher fidelity adder than permitted by onset control alone, allowing *C. crescentus* to better maintain its size in the face of biological noise.

RESULTS

Perturbing Constriction Rate Changes the Cell Length

To test the role of constriction, we perturbed its rate pharmacologically and genetically. Fosfomycin ([(2R,3S)-3-methyloxiran-2-yl]phosphonic acid) inhibits the PG synthesis enzyme MurA (Kahan et al., 1974), which slows PG synthesis and therefore the constriction rate. In addition, the divisome includes cell wall remodeling enzymes, including the late-arriving FtsW and FtsI. Several point mutants of the glycosyltransferase FtsW (Meeske et al., 2016) and its cognate transpeptidase FtsI (Adam et al., 1997), referred to as FtsW**I*, resulted in a gain-of-function phenotype in *C. crescentus* (Modell et al., 2014). It was hypothesized that these mutations maintain the enzymes in their active state, and thereby would increase the constriction rate (Modell et al., 2014).

We resolved cell shape dynamics during the cell cycle by performing dual-color imaging of the inner membrane and divisome proteins (FtsZ-GFP, FtsW-GFP) with time-lapse SIM (Figure 1A; Videos S1, S2, and S3; Transparent Methods; and Key Resource Table) on a synchronized population of cells. We used automated image analysis to quantify cell shape parameters during the cell cycle (Figures 1B and S1, Transparent Methods). The overall cell length relative to the wild-type (WT) strain was shorter for FtsW**I* and longer for fosfomycin-treated cells (Figures 2A, S2A, and S2B), consistent with previous studies (Harris and Theriot, 2016; Modell et al., 2014).

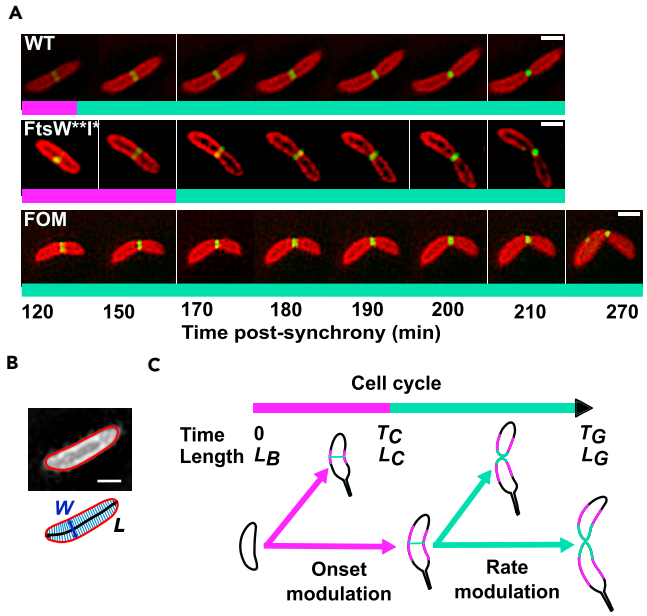

Figure 1. Experimental Strategy and Constriction-Related Models for Modulation of Cell Size

(A) Time-lapse SIM images: inner membrane (mCherry-MTS2, red) and FtsZ (FtsZ-GFP, green). Shown are example wild-type (WT), FtsW**I* mutant, and fosfomycin-treated cells through constriction, until separation. Images were bleach corrected for visualization, see Transparent Methods.

(B) Analysis of cell shape parameters using sDaDa (see Transparent Methods and Figure S1): the central line (black) is used to measure length (L), the width (W) is extracted from each perpendicular segment, and the cell contour defines cell shape (red line).

(C) Constriction rate or onset control mechanisms for length. Cells are born at time 0 with length at birth L_B and elongate exponentially. T_C and L_C are the time and length at constriction onset. T_G and L_G are the time and length at the end of the cell cycle. Magenta parts of the cell contour represent lateral elongation, and cyan parts represent septal elongation. Scale bars: 500 nm. Bicolor bars indicate the stage: pre-constriction (magenta) and post-constriction (cyan). See also Figure S1.

Could elongation before the onset of constriction (Figure 1C, onset modulation) set the differences in final length between FtsW**I* mutant, fosfomycin-treated, and WT cells? The appearance of a measurable constriction in SIM data corresponded well with the arrival of FtsW (Figure S1C) and allowed us to separate elongation before and after constriction onset. Differences in elongation before constriction for all conditions (Figure 2B) were insufficient to account for the observed differences in final length (Figure 2A). Thus, we examined shape changes during constriction (Figure 1C). Individual cells continued to elongate exponentially with the same apparent rate, even as they changed from pure elongation to mid-cell remodeling and constriction (Figures 2C and 2E). However, the mean constriction rate was increased for the FtsW**I* mutant and decreased for fosfomycin-treated cells when compared with WT (Figure 2C), leading to differences in overall cell elongation during constriction (Figure 2D). We also examined the impact of MreB on cell size control using the point mutant MreBQ26P (Aaron et al., 2007), which participates only in side-wall elongation and not in septal elongation. We found that cells were longer on average than WT, with a higher elongation rate, indicating that this is a gain-of-function mutation. Interestingly, the average constriction rate increased, resulting in a nearly unchanged elongation during constriction (Figure S2D). Thus, we have demonstrated that constriction rate modulation can be a mechanism for cell size control, independent of onset modulation (Taheri-Araghi et al., 2015; Weart et al., 2007) or elongation.

We found that individual cells continued to elongate at the same rate before and during constriction, although different perturbations modulated their constriction rate. Thus, faster constriction as in the case of FtsW**I* implies that cells should have shorter, blunter poles, whereas slower constriction as in the case of fosfomycin treatment implies that they should have longer, sharper poles. Indeed, kymographs show a more extended gradient in cell width at the poles of fosfomycin-treated cells (Figure 2E). In contrast, FtsW**I* cells show a steeper gradient at the poles. This was confirmed quantitatively by measuring the radius of curvature at the poles (Figure 2F). Furthermore, a population-wide analysis of pole shape

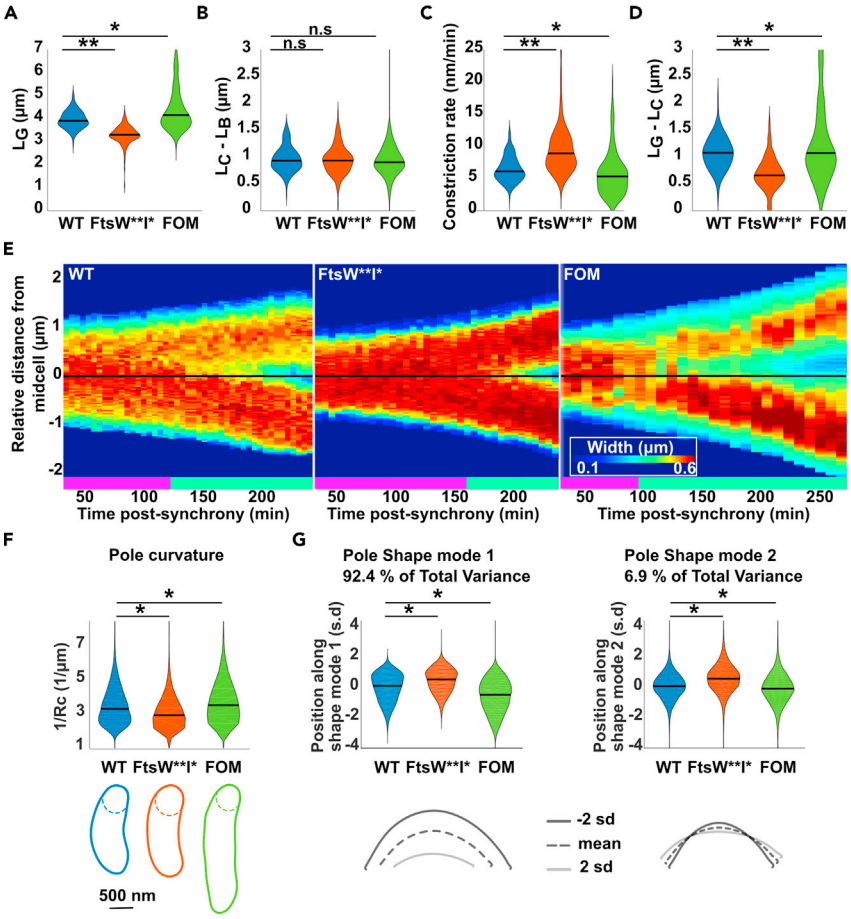

Figure 2. Differences in Constriction Rate Yield Different Cell Sizes and Pole Shapes

(A–D) Single-cell distributions of (A) length at division, (B) elongation before constriction, (C) mean constriction rate, and (D) elongation during constriction. (A–D), black bars represent the median of the population. Number of cells WT: N = 208; FtsW**I*: N = 212; FOM: N = 220. **p < 0.005, *p < 0.05, n.s., not significant.

(E) Kymographs of representative cells, displaying cell diameter along the cell's length (vertical axis) versus growth time post-synchrony (horizontal axis); red indicates large diameter, blue indicates small diameter. The middle of the cell is indicated by the black horizontal line. Bicolor bars indicate the stage: pre-constriction (magenta) and post-constriction (cyan).

(F) Pole shape analysis. The curvature is the reciprocal of the radius (Rc) of a circle tangent to the curve at a given point, here taken to be the pole. Each cell contour represents a representative single cell from each condition; the distribution of curvatures is plotted above (median value, black bar). *p<0.05.

(G) The pole region was extracted from each contour (>6,000 cells per condition) and analyzed using principal component analysis (Celltool [Pincus and Theriot, 2007]). Shape mode 1 mostly accounts for variation in the length of the pole; shape mode 2 mostly accounts for variation in the bluntness of the pole independent of length. The distributions of each shape mode are plotted, with examples of corresponding shapes. *p<0.05.

See also Figure S2.

demonstrated that over 95% of the total shape variance is accounted for with two principle shape modes, which primarily capture variation in the length and bluntness of the poles (Figure 2G). FtsW**I*, fosfomycin-treated, and WT cells were all distinct along each of these shape axes. We also observed differences in the width of the Z-ring, which appears laterally extended in the fosfomycin case (Figure S2C). This may result from changes in length at constriction onset, since the region of lowest MipZ concentration will be more extended in longer cells (Thanbichler and Shapiro, 2006).

Constriction Rate Modulation Balances Elongation before and during Constriction

To better decipher the relative role of the constriction rate in cell size regulation, we further analyzed its contribution to cell size homeostasis. Our experiments were designed to precisely measure the relative

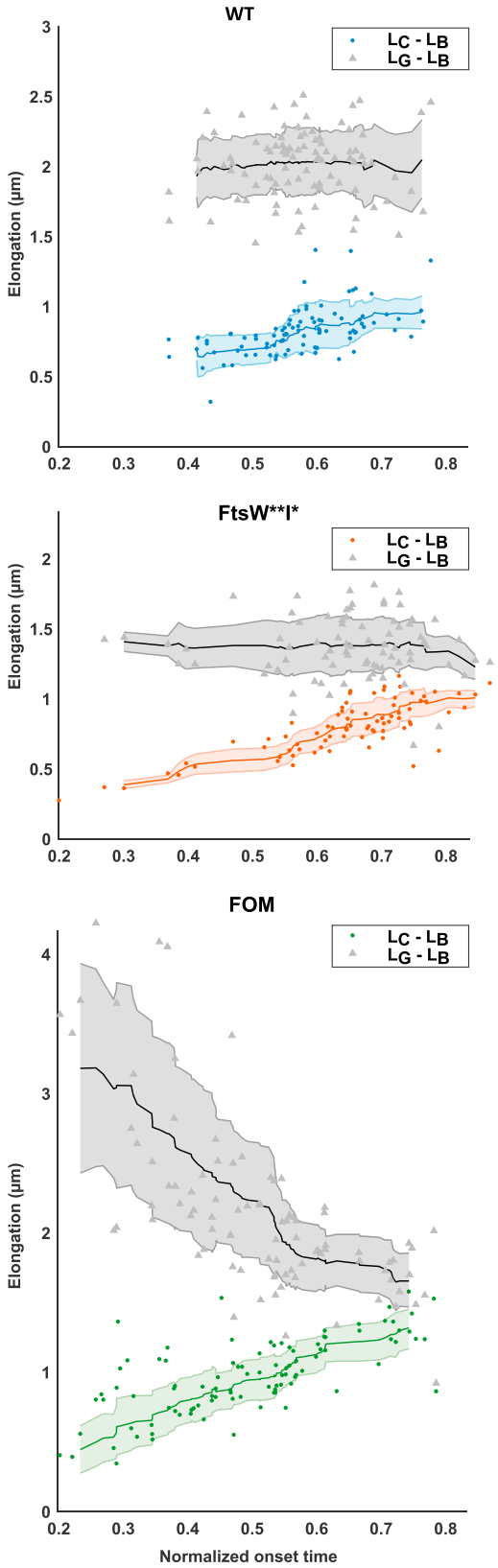
WT
LC - LB
LG - LB
Elongation (µm)
FtsW**I*
LC - LB
LG - LB
Elongation (µm)
FOM
LC - LB
LG - LB
Elongation (µm)
Normalized onset time

Figure 3. Compensation of Elongation Before and During Constriction Contributes to Cell Size Homeostasis
Total elongation (gray) and elongation before constriction (color) for individual wild-type, FtsW**I*, and fosfomycin (FOM)-treated cells, as a function of normalized onset time (T_C/T_G). Lines represent the 20 cells moving average; the shaded zones represent the moving SD. Extreme outliers, more than 2 standard deviations from the mean, were omitted for the calculation of the moving average. See also Figure S3.

contributions to total elongation, and not to distinguish between different general models of homeostasis, which would require measurement over thousands of generations. We found that cells elongated with a distinct mean value for each condition (Figure 3), and that the more individual cells elongated before, the less they elongated during constriction across all conditions tested, including in *E. coli* WT cells (Figures 3 and S3). Indeed, the total elongation was independent of the relative time that the cells spent in elongation and constriction phases, with the exception of fosfomycin-treated cells (Figure 3), generally consistent with an "adder." Consequently, the variance in total elongation was lower than the variances in elongation before and during constriction would have independently suggested. This was true for all populations, including under perturbed conditions (Figure S3A). These results demonstrate compensation, or over-compensation in the case of fosfomycin (Figures 3 and S3B), between elongation before and during constriction, resulting in a higher fidelity homeostasis for total elongation (Figures S3A–S3C).

What could be the mechanism for this compensation? Elongation and constriction rates together determine elongation during constriction. Compensation could occur if cells that elongate less before onset subsequently elongate more rapidly or constrict more slowly. However, elongation rate during constriction did not negatively correlate with elongation before constriction (Figure S4A). To better understand constriction dynamics, we examined single cell waist widths as a function of relative duration of constriction (Figure 4A). Cells that elongated more before constriction also spent relatively less time constricting, indicating a higher overall constriction rate. The converse was true for cells that elongated less before constriction, but this observation alone does not rule out the possibility of a very late regulatory step being responsible for changes in average constriction rate. Single cells constricted with increasing rate until division; thus, we defined two rates, corresponding to early and late constriction (Figure S4B), similar to Banerjee et al. (2017). Interestingly, early constriction rate correlated positively with elongation before constriction, but late rate did not (Figures 4B and 4C). Hence, early constriction rate changes at the single-cell level to adjust elongation during and compensate elongation before constriction.

Although molecular mechanisms have been proposed for ensuring homeostasis, the identity of the underlying regulatory factors remains controversial. A previous model estimated PG precursor excess amount as a function of cell cycle (Harris and Theriot, 2016). Each cell is assumed to be born with negligible excess and generates an increasing excess of PG precursors during elongation. PG precursors are synthesized in the cell volume, at a volume-dependent rate, while being depleted as they become integrated into the cell wall (see Transparent Methods, Estimation of Excess Peptidoglycan Precursor). Using this model and experimentally measured cell contours to estimate the changes in surface area (ΔA) and volume (ΔV), we calculated the excess precursor area (A_{excess}) at the onset of constriction (T_c) for individual cells at the onset of constriction:

$$A_{excess}(T_c) = \left\langle \frac{\Delta A}{\Delta V} \right\rangle_{cell\ cycle} \Delta V(T_c) - \Delta A(T_c)$$

Here, $\langle\rangle_{cell\ cycle}$ refers to the value averaged over the cell cycle. Since it took on average 30 min to set up each experiment, we underestimated the volume and area at birth, leading to an offset toward negative estimated precursor excess (Figure 4D). However, we expect the trends to be insensitive to this shift.

DISCUSSION

To explain our findings of constriction rate modulation dependent on elongation, we speculate on a parsimonious model in which PG precursor excess also sets the rate of PG remodeling at the constriction site, and therefore the rate of constriction: the higher the excess, the shorter the constriction duration. Indeed, we observed a positive correlation between the early rate of constriction and estimated excess PG precursor for WT and FtsW**I* cells (Figures 4D and S4). This is also consistent with measurements of

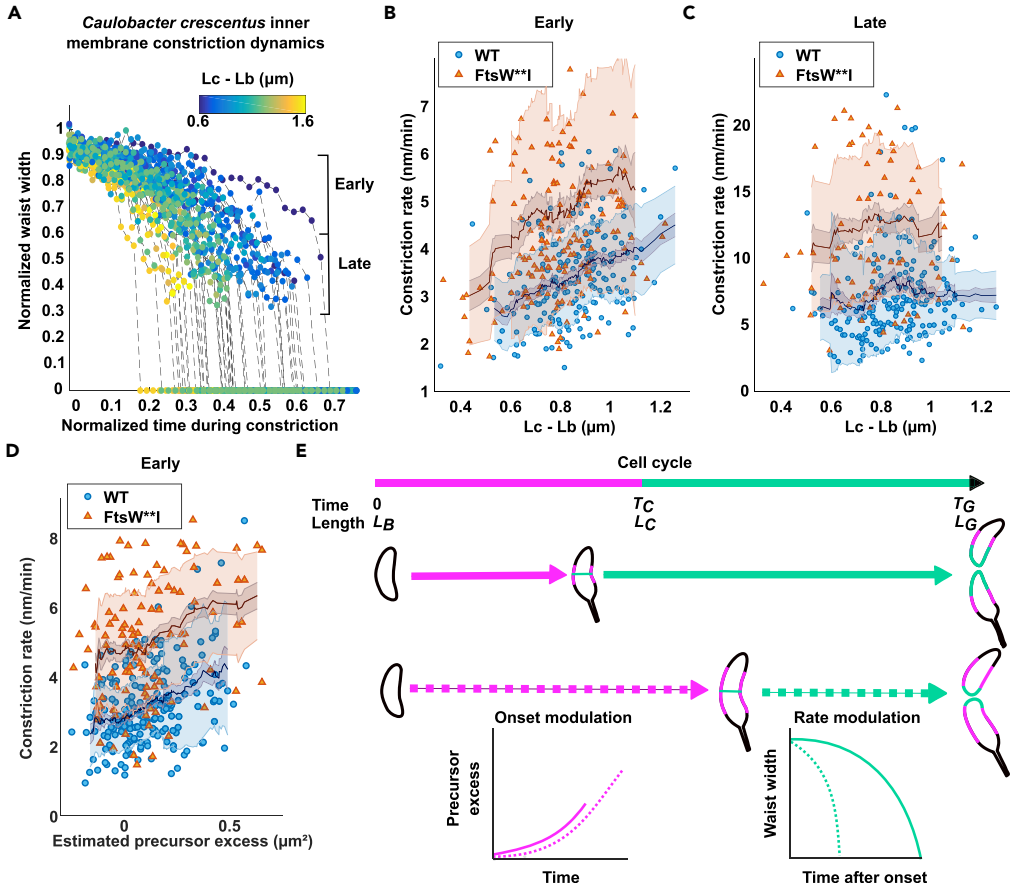

Figure 4. Early Constriction Rates Compensate for Elongation Before Onset

(A) Normalized waist width as a function of normalized time during constriction, color map represents the elongation before constriction. The measurable constriction was divided into early (0.9–0.6) and late (0.6–0.3) stages.

(B) Testing correlation between early constriction rate and elongation before constriction in both WT and mutant strains; WT: r = 0.45, p value < 0.01; mutant: r = 0.24, p value < 0.01 (Pearson correlation coefficient).

(C) Testing correlation between late constriction rate and elongation before constriction; WT: r = 0.05, p value > 0.48; mutant: r = 0.02, p value > 0.8 (Pearson correlation coefficient).

(D) Testing correlation between estimated PG precursor excess and early constriction rate, WT: r = 0.33, p value < 0.01; mutant: r = 0.29, p value < 0.01 (Pearson correlation coefficient). N ≥ 200 for each strain. Lines in (B–D) represent the 20-cells moving average; the shaded zones represent the moving SD. Extreme outliers, more than 2 standard deviations from the mean, were omitted for the calculation of the moving average.

(E) Schematic of size regulation in *C. crescentus* with mixed modulation of constriction onset and rate. Magenta parts of the cell contour represent lateral elongation, and cyan parts represent septal elongation. Later onset leads to higher PG precursor excess, which drives more rapid initial constriction (dashed trajectories), and vice versa.

See also Figure S4.

compensation in the MreBQ26P mutant, in which cells elongate faster. According to this model, an increased elongation rate with a constant PG precursor production rate implies that cells will be longer when they achieve a critical concentration to initiate constriction, without disrupting compensation. This is consistent with our findings (Figure S3E), indicating that MreB does not play a major role in setting constriction rates. Furthermore, as the new cell poles are built, the excess PG precursor should diminish, leading to a decreased creation of area per time. This is indeed what we observe (see Transparent Methods, Empirical Constriction Model), consistent with models of constriction rate in *E. coli* (Coltharp et al., 2016). We also observed a positive correlation between the overall rate of constriction and elongation before constriction in *E. coli* (Figure S3F), although we were not able to independently verify early and late constriction rates. Fosfomycin inhibits PG synthesis, so we can no longer use the same mathematical expression to estimate precursor excess, since the activity of fosfomycin would introduce an extra

depletion term. Interestingly, within our model, this should lead to a slower constriction, consistent with our observations (Figure 2C).

Although we have posed the regulatory factor to be PG precursors, this remains controversial because there is only indirect evidence for their role. Any "X-factor" regulatory molecule for constriction rate following the functional relationship described for surface area and volume would fit within the model we suggest. On the other hand, cells that do not elongate during the constriction phase should be insensitive to constriction rate compensation. Within the context of "size homeostasis," this proposed mechanism neither precludes nor requires any given overall model, but does suggest a means to achieve higher fidelity in adder-type models. The fact that this compensation occurs as a late step in cell cycle is consistent with the analysis of the adder, which was shown to require a regulatory step after the assembly of the Z-ring, during the constriction stage (Campos et al., 2014).

Under nutrient-enriched growth conditions, *Salmonella*, *E. coli*, and *B. subtilis* can coordinate their cell size with nutrient availability, perhaps to allow sufficient room for multi-fork replication (Donachie and Begg, 1989; Sargent, 1975; Schaechter et al., 1958) and a concomitant increase in cell size to maintain a constant volume per origin (Amir, 2017; Zheng et al., 2016). Remarkably, *C. crescentus* shows no such nutrient adaptation (Beaufay et al., 2015; Campos et al., 2014), and how its size is modulated in the face of mutations or pharmacological perturbations has remained a mystery. Our findings show a clear contribution to cell size control from growth during the final constriction stage of the cell cycle. Modulation of constriction dynamics changes the overall length of cells, in a manner that has implications for cell shape. In the hypothetical case of extremely rapid constriction, the cell length would be set almost entirely by the growth during the pure elongation stage, leading to short cells with blunt poles. By modulating constriction onset and rate together (Figure 4E), cells may arrive at a variety of pole shapes, an emerging control mechanism for bacterial cell shape (Lariviere et al., 2018).

Intriguingly, the cell wall itself can have differential properties at the division site. In *B. subtilis*, the division septum has an enrichment of pentapeptides compared with the rest of the cell envelope (Morales Angeles et al., 2017), perhaps due to a change in the cross-linking or PG composition. In *E. coli*, glycan strands lacking stem peptides are enriched at the septum, allowing proteins containing the PG binding (SPOR) domain to be recruited (Yahashiri et al., 2015). In *C. crescentus*, the hydrolase DipM is recruited to the division site by its PG binding LysM domains, suggesting a distinct PG chemistry (Goley et al., 2010; Möll et al., 2010; Poggio et al., 2010). Consistently, we observed a differential, reduced staining by wheat germ agglutinin at mid-cell for later stages of the cell (Figure S4I) (Douglass et al., 2016). We expect that in future studies it will be important to use fluorescent cell-cycle markers in conjunction with fluorescent D-amino acids (Kuru et al., 2012), which together can identify cell-cycle timing and modes of growth. It would be interesting to investigate whether the rate of constriction also affects the cell wall chemistry at the division site.

Different factors have been demonstrated to be important for determining constriction dynamics. Before cells can build a septal wall, chromosomes must be partitioned; accordingly, machinery that coordinates the two, such as MatP in *E. coli*, can also modulate constriction rate (Coltharp et al., 2016). Similarly, dynamically treadmilling FtsZ filaments act as a scaffold to direct cell wall remodelers to the division site and can modulate their rate (Bisson-Filho et al., 2017; Lariviere et al., 2018; Yang et al., 2017). Nevertheless, the activity of PG remodeling enzymes involved in constriction might depend on PG precursor concentrations and thus may act as a part of a responsive machine. The PG remodeling enzymes FtsW and MurJ are both proposed to act as lipid II flippases (Meeske et al., 2015; Mohammadi et al., 2011); intriguingly, in *Staphylococcus aureus*, MurJ recruitment was recently shown to coincide with a second, late constriction stage in which the constriction rate shows reduced sensitivity to chemical inhibition of FtsZ dynamics (Monteiro et al., 2018). Similarly, we have shown that mutations to FtsW can increase the constriction rates in *C. crescentus*, an organism in which biphasic constriction was also reported (Banerjee et al., 2017). Since, for individual cells, elongation proceeds exponentially with a single rate constant even as PG precursor excess is predicted to increase over the cell cycle, the elongation machinery is presumably relatively insensitive to changes in PG precursor amounts. By coupling the elongation machinery to the PG precursor-sensitive constriction machinery, the cell may have arrived at a simple means of compensating for fluctuations in elongation during different phases of the cell cycle. Consistent with this, others have proposed that septal and lateral PG synthesis draws precursors from the same pool, allowing communication to occur between the two processes (Harris and Theriot, 2016; Woldringh et al., 1987). This compensation still has its

limitations as we observed in the case of FtsW**I* (Figure S3B); in the case of large elongation before onset, cells must still elongate by a minimum amount during Z-ring maturation (Figure S2C) and constriction. In the future, it will be interesting to identify the molecular partners responsible for constriction rate modulation and PG sensing, and to experimentally investigate the mechanism behind compensation of elongation.

METHODS

All methods can be found in the accompanying Transparent Methods supplemental file.

DATA AND SOFTWARE AVAILABILITY

All data and software used to support the results of this manuscript are available from the Lead Contact upon reasonable request. Original data is available on Zenodo, DOI: 10.5281/zenodo.1248441 and 10.5281/zenodo.1241005. Software is available on Zenodo, DOI: 10.5281/zenodo.1173751 and on github: https://github.com/LEB-EPFL/sDaDa.

SUPPLEMENTAL INFORMATION

Supplemental Information includes Transparent Methods, four figures, and three videos and can be found with this article online at https://doi.org/10.1016/j.isci.2018.05.020.

ACKNOWLEDGMENTS

The authors would like to thank Jan Skotheim and Devon Chandler-Brown for critical reading of the manuscript, Thierry Laroche from the EPFLBioimaging and Optics Core Facility (EPFL-BIOP) for support in imaging, Manley lab members and Collier lab members for helpful discussions, and the Thanbichler lab and Christine Jacobs Wagner Lab for plasmid gifts. This work was supported by the Swiss National Science Foundation Project Grant CR32I3_166330 (S.M.), European Research Council Starting Grant 243016 (S.M.), and Marie Curie Intra-European Fellowship PIEF-GA-2011-297918 (S.H.).

AUTHOR CONTRIBUTIONS

Conceptualization, A.L., A.V., S.M., E.G., M.T.L., and S.H.; Methodology, A.L., A.V., S.M., E.G., M.T.L., S.H., and A.A.; Software, A.V., A.A., F. S., S.H., Z.P., and A.L.; Validation, A.L., A.V., S.M., S.H., and A.A.; Formal Analysis, A.V., A.A., S.H., Z.P., A.L., and S.M; Investigation, A.L., A.V., E.G., and S.H.; Resources, E.G., M.T.L., and S.M.; Data Curation, A.V., A.L., and A.A.; Writing – Original Draft, S.M., A.L, A.V., and A.A.; Writing – Review & Editing, all authors.; Visualization, A.L., A.V., A.A., Z.P., and S.M.; Supervision, S.M., E.G., A.L., and S.H.; Funding Acquisition, S.M. and S.H.

DECLARATION OF INTERESTS

The authors declare no competing interests.

Received: February 13, 2018
Revised: May 4, 2018
Accepted: May 24, 2018
Published: June 29, 2018

REFERENCES

Aaron, M., Charbon, G., Lam, H., Schwarz, H., Vollmer, W., and Jacobs-Wagner, C. (2007). The tubulin homologue FtsZ contributes to cell elongation by guiding cell wall precursor synthesis in *Caulobacter crescentus*. Mol. Microbiol. *64*, 938–952.

Adam, M., Fraipont, C., Rhazi, N., Nguyen-Distèche, M., Lakaye, B., Frère, J.M., Devreese, B., Van Beeumen, J., van Heijenoort, Y., van Heijenoort, J., et al. (1997). The bimodular G57-V577 polypeptide chain of the class B penicillin-binding protein 3 of *Escherichia coli* catalyzes peptide bond formation from thiolesters and does not catalyze glycan chain polymerization from the lipid II intermediate. J. Bacteriol. *179*, 6005–6009.

Amir, A. (2017). Point of View: is cell size a spandrel? Elife *6*, e22186.

Banerjee, S., Lo, K., Daddysman, M.K., Selewa, A., Kuntz, T., Dinner, A.R., and Scherer, N.F. (2017). Biphasic growth dynamics control cell division in Caulobactercrescentus. Nat. Microbiol. *2*, 17116.

Beaufay, F., Coppine, J., Mayard, A., Laloux, G., De Bolle, X., and Hallez, R. (2015). A NAD-dependent glutamate dehydrogenase coordinates metabolism with cell division in *Caulobacter crescentus*. EMBO J. *34*, 1786–1800.

Beveridge, T.J. (1988). The bacterial surface: general considerations towards design and function. Can. J. Microbiol. *34*, 363–372.

Bisson-Filho, A.W., Hsu, Y.-P., Squyres, G.R., Kuru, E., Wu, F., Jukes, C., Sun, Y., Dekker, C., Holden, S., Van Nieuwenhze, M.S., et al. (2017). Treadmilling by FtsZ filaments drives peptidoglycan synthesis and bacterial cell division. Science *355*, 739–743.

Campos, M., Surovtsev, I.V., Kato, S., Paintdakhi, A., Beltran, B., Ebmeier, S.E., and Jacobs-Wagner, C. (2014). A constant size extension drives bacterial cell size homeostasis. Cell *159*, 1433–1446.

Coltharp, C., Buss, J., Plumer, T.M., and Xiao, J. (2016). Defining the rate-limiting processes of bacterial cytokinesis. Proc. Natl. Acad. Sci. USA *113*, E1044–E1053.

Cooper, S., and Helmstetter, C.E. (1968). Chromosome replication and the division cycle of *Escherichia coli* B/r. J. Mol. Biol. *31*, 519–540.

den Blaauwen, T., Hamoen, L.W., and Levin, P.A. (2017). The divisome at 25: the road ahead. Curr. Opin. Microbiol. *36*, 85–94.

Donachie, W.D., and Begg, K.J. (1989). Cell length, nucleoid separation, and cell division of rod-shaped and spherical cells of *Escherichia coli*. J. Bacteriol. *171*, 4633–4639.

Douglass, K.M., Sieben, C., Archetti, A., Lambert, A., and Manley, S. (2016). Super-resolution imaging of multiple cells by optimized flat-field epi-illumination. Nat. Photonics *10*, 705–708.

Goley, E.D., Comolli, L.R., Fero, K.E., Downing, K.H., and Shapiro, L. (2010). DipM links peptidoglycan remodeling to outer membrane organization in *Caulobacter*. Mol. Microbiol. *77*, 56–73.

Gustafsson, M.G.L. (2000). Surpassing the lateral resolution limit by a factor of two using structured illumination microscopy. J. Microsc. *198*, 82–87.

Harris, L.K., and Theriot, J.A. (2016). Relative rates of surface and volume synthesis set bacterial cell size. Cell *165*, 1479–1492.

Ho, P.-Y., and Amir, A. (2015). Simultaneous regulation of cell size and chromosome replication in bacteria. Front. Microbiol. *6*, 662.

Jun, S., and Taheri-Araghi, S. (2015). Cell-size maintenance: universal strategy revealed. Trends Microbiol. *23*, 4–6.

Kahan, F.M., Kahan, J.S., Cassidy, P.J., and Kropp, H. (1974). The mechanism of action of fosfomycin (phosphonomycin). Ann. N. Y. Acad. Sci. *235*, 364–386.

Koch, A.L. (1996). What size should a bacterium be? A question of scale. Annu. Rev. Microbiol. *50*, 317–348.

Kuru, E., Hughes, H.V., Brown, P.J., Hall, E., Tekkam, S., Cava, F., De, P., Brun, Y.V., and Vannieuwenhze, M.S. (2012). In situ probing of newly synthesized peptidoglycan in live bacteria with fluorescent D-amino acids. Angew. Chem. Int. Ed. *51*, 12519–12523.

Lariviere, P.J., Szwedziak, P., Mahone, C.R., Löwe, J., and Goley, E.D. (2018). FzlA, an essential regulator of FtsZ filament curvature, controls constriction rate during *Caulobacter* division. Mol. Microbiol. *107*, 180–197.

Laub, M.T., McAdams, H.H., Feldblyum, T., Fraser, C.M., and Shapiro, L. (2000). Global analysis of the genetic network controlling a bacterial cell cycle. Science *290*, 2144–2148.

Leitao, R.M., and Kellogg, D.R. (2017). The duration of mitosis and daughter cell size are modulated by nutrients in budding yeast. J.Cell. Biol. *216*, 3463–3470.

Marczynski, G.T. (1999). Chromosome methylation and measurement of faithful, once and only once per cell cycle chromosome replication in *Caulobacter crescentus*. J. Bacteriol. *181*, 1984–1993.

Meeske, A.J., Sham, L.-T., Kimsey, H., Koo, B.-M., Gross, C.A., Bernhardt, T.G., and Rudner, D.Z. (2015). MurJ and a novel lipid II flippase are required for cell wall biogenesis in *Bacillus subtilis*. Proc. Natl. Acad. Sci. USA *112*, 6437–6442.

Meeske, A.J., Riley, E.P., Robins, W.P., Uehara, T., Mekalanos, J.J., Kahne, D., Walker, S., Kruse, A.C., Bernhardt, T.G., and Rudner, D.Z. (2016). SEDS proteins are a widespread family of bacterial cell wall polymerases. Nature *537*, 634–638.

Modell, J.W., Kambara, T.K., Perchuk, B.S., and Laub, M.T. (2014). A DNA damage-Induced, SOS-independent checkpoint regulates cell division in *Caulobacter crescentus*. PLoS Biol. *12*, e1001977.

Mohammadi, T., van Dam, V., Sijbrandi, R., Vernet, T., Zapun, A., Bouhss, A., Diepeveen-de Bruin, M., Nguyen-Distèche, M., de Kruijff, B., and Breukink, E. (2011). Identification of FtsW as a transporter of lipid-linked cell wall precursors across the membrane. EMBO J. *30*, 1425–1432.

Möll, A., Schlimpert, S., Briegel, A., Jensen, G.J., and Thanbichler, M. (2010). DipM, a new factor required for peptidoglycan remodelling during cell division in *Caulobacter crescentus*. Mol. Microbiol. *77*, 90–107.

Monteiro, J.M., Pereira, A.R., Reichmann, N.T., Saraiva, B.M., Fernandes, P.B., Veiga, H., Tavares, A.C., Santos, M., Ferreira, M.T., Macário, V., et al. (2018). Peptidoglycan synthesis drives an FtsZ-treadmilling-independent step of cytokinesis. Nature *554*, 528–532.

Morales Angeles, D., Liu, Y., Hartman, A.M., Borisova, M., de Sousa Borges, A., de Kok, N., Beilharz, K., Veening, J.-W., Mayer, C., Hirsch, A.K.H., et al. (2017). Pentapeptide-rich peptidoglycan at the *Bacillus subtilis* cell-division site. Mol. Microbiol. *104*, 319–333.

National Research Council (US) Steering Group for the Workshop on Size Limits of Very Small Microorganisms (1999). Size Limits of Very Small Microorganisms: Proceedings of a Workshop (National Academies Press (US)).

Osella, M., Nugent, E., and Cosentino Lagomarsino, M. (2014). Concerted control of *Escherichia coli* cell division. Proc. Natl. Acad. Sci. USA *111*, 3431–3435.

Pincus, Z., and Theriot, J.A. (2007). Comparison of quantitative methods for cell-shape analysis. J. Microsc. *227*, 140–156.

Poggio, S., Takacs, C.N., Vollmer, W., and Jacobs-Wagner, C. (2010). A protein critical for cell constriction in the Gram-negative bacterium *Caulobacter crescentus* localizes at the division site through its peptidoglycan-binding LysM domains. Mol. Microbiol. *77*, 74–89.

Reshes, G., Vanounou, S., Fishov, I., and Feingold, M. (2008). Timing the start of division in *E. coli*: a single-cell study. Phys. Biol. *5*, 046001.

Sargent, M.G. (1975). Control of cell length in *Bacillus subtilis*. J. Bacteriol. *123*, 7–19.

Schaechter, M., Maaloe, O., and Kjeldgaard, N.O. (1958). Dependency on medium and temperature of cell size and chemical composition during balanced grown of *Salmonella typhimurium*. J. Gen. Microbiol. *19*, 592–606.

Schulz, H.N., and Jørgensen, B.B. (2001). Big bacteria. Annu. Rev. Microbiol. *55*, 105–137.

Skerker, J.M., and Laub, M.T. (2004). Cell-cycle progression and the generation of asymmetry in *Caulobacter crescentus*. Nat. Rev. Microbiol. *2*, 325–337.

Sompayrac, L., and Maaløe, O. (1973). Autorepressor model for control of DNA replication. Nat. New Biol. *241*, 133.

Taheri-Araghi, S., Bradde, S., Sauls, J.T., Hill, N.S., Levin, P.A., Paulsson, J., Vergassola, M., and Jun, S. (2015). Cell-size control and homeostasis in bacteria. Curr. Biol. *25*, 385–391.

Thanbichler, M., and Shapiro, L. (2006). MipZ, a spatial regulator coordinating chromosome segregation with cell division in *Caulobacter*. Cell *126*, 147–162.

Wallden, M., Fange, D., Lundius, E.G., Baltekin, Ö., and Elf, J. (2016). The synchronization of replication and division cycles in individual *E. coli* cells. Cell *166*, 729–739.

Wang, P., Robert, L., Pelletier, J., Dang, W.L., Taddei, F., Wright, A., and Jun, S. (2010). Robust growth of *Escherichia coli*. Curr. Biol. *20*, 1099–1103.

Weart, R.B., Lee, A.H., Chien, A.-C., Haeusser, D.P., Hill, N.S., and Levin, P.A. (2007). A metabolic sensor governing cell size in bacteria. Cell *130*, 335–347.

Woldringh, C.L., Huls, P., Pas, E., Brakenhoff, G.J., and Nanninga, N. (1987). Topography of division peptidoglycan synthesis during elongation and polar cap formation in a cell mutant of *Escherichia coli* MC4100. Microbiology *133*, 575–586.

Yahashiri, A., Jorgenson, M.A., and Weiss, D.S. (2015). Bacterial SPOR domains are recruited to septal peptidoglycan by binding to glycan strands that lack stem peptides. Proc. Natl. Acad. Sci. USA *112*, 11347–11352.

Yang, X., Lyu, Z., Miguel, A., McQuillen, R., Huang, K.C., and Xiao, J. (2017). GTPase activity-coupled treadmilling of the bacterial tubulin FtsZ organizes septal cell wall synthesis. Science *355*, 744–747.

Zheng, H., Ho, P.-Y., Jiang, M., Tang, B., Liu, W., Li, D., Yu, X., Kleckner, N.E., Amir, A., and Liu, C. (2016). Interrogating the *Escherichia coli* cell cycle by cell dimension perturbations. Proc. Natl. Acad. Sci. USA *113*, 15000–15005.

ISCI, Volume *4*

Supplemental Information

Constriction Rate Modulation Can Drive Cell Size Control and Homeostasis in *C. crescentus*

Ambroise Lambert, Aster Vanhecke, Anna Archetti, Seamus Holden, Felix Schaber, Zachary Pincus, Michael T. Laub, Erin Goley, and Suliana Manley

SUPPLEMENTAL FIGURES

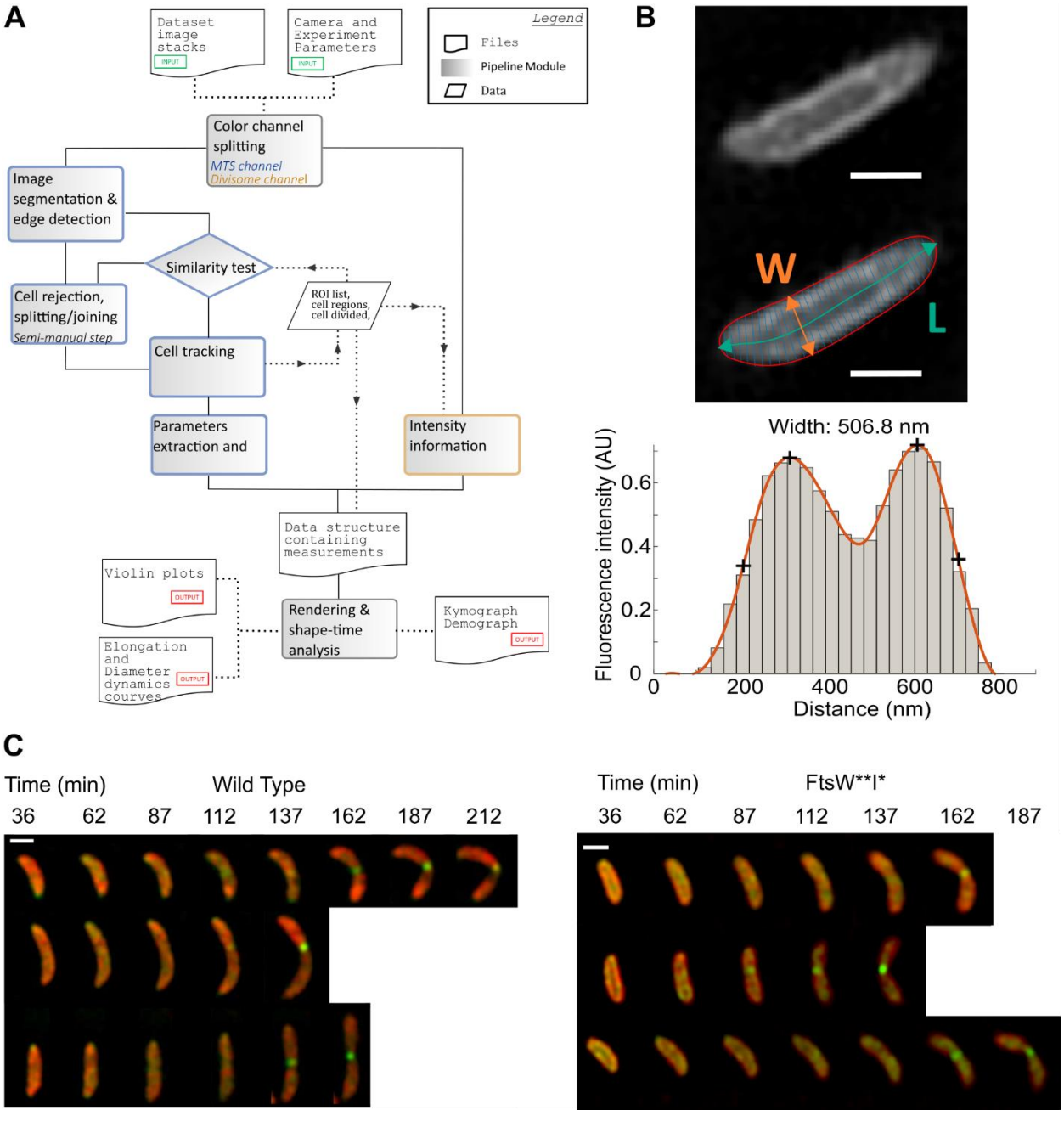

Figure S1. Image analysis pipeline, Related to Figure 1.
(**A**) Analysis software flowchart. (**B**) Analysis of SIM images inner membrane label: from the raw data, the centerline is calculated. At equally spaced points along the centerline, the width is measured by extracting the intensity profile along a line (thin cyan colored line) perpendicular to the centerline (thick cyan colored line) at that point (top panel red line represent the contour). Lower panel: The extracted intensity profile (grey bars) is smoothed by fitting a spline (orange line lower panel). The maxima are calculated (top plus signs on orange line), and the outer position with the half-maximum value is found (lower plus sign on orange line). The distance between these two positions is defined as the width. Scale bar: 700 nm. (**C**) SIM images of FtsW onset. Red inner membrane MTS2-mCherry labeled, FtsW-GFP label Every one in

five frames is shown for three representative cells for Wild Type and FtsW**I*. Images were bleach corrected for visualization, see Transparent Methods. Scale bar: 1 μm.

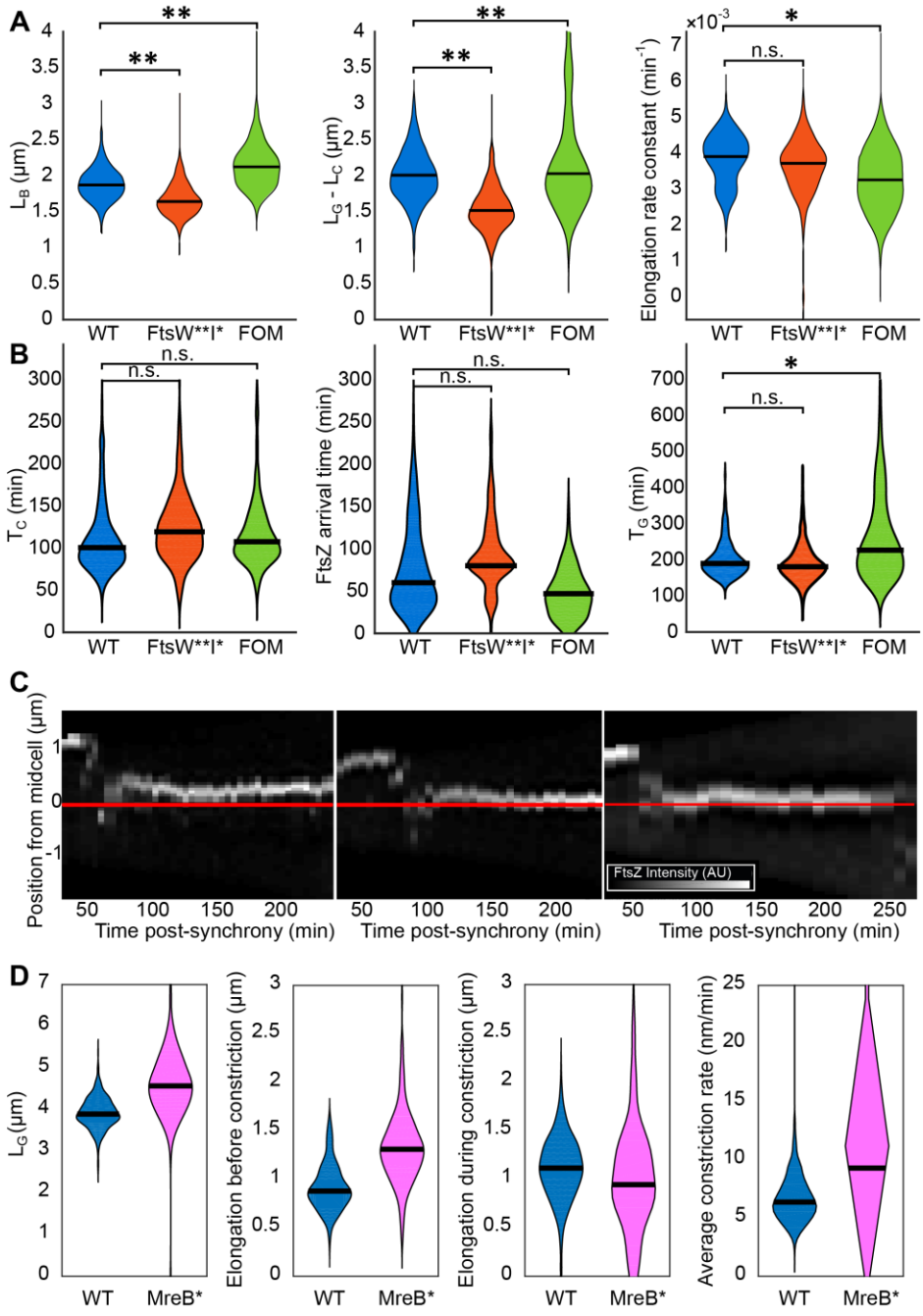
A
B
C
D
L_B (μm)
L_G - L_C (μm)
Elongation rate constant (min^{-1})
T_C (min)
FtsZ arrival time (min)
T_G (min)
WT
FtsW**I*
FOM
n.s.
Position from midcell (μm)
Time post-synchrony (min)
FtsZ Intensity (AU)
L_G (μm)
Elongation before constriction (μm)
Elongation during constriction (μm)
Average constriction rate (nm/min)
MreB*

Figure S2. Differences in size and elongation rate between populations, Related to Figure 2.
(A) From left to right**:** Violin plots distributions of length at birth, Violin plots distributions of total elongation, Violin plots distributions of elongation rate constant, (**B**) From left to right: Violin plots distributions of onset of constriction, Violin plots distributions of FtsZ arrival time and Violin plots distributions of generation time for the WT, FtsW**I* and fosfomycin treated WT populations. Black horizontal bars represent the median. N: for (**A-B,**): WT: 406, FtsW**I*: 357, FOM: 203, for Significance: **: $p<0.005$, *: $p<0.05$, n.s.: not significant. (**C**) Kymographs of representative cells: FtsZ-GFP intensity distribution along the cell's length (vertical axis), versus cell cycle time (horizontal axis). (**D**) From left to right: Violin plots comparison of WT versus MreB* mutant comparison of Length at division, elongation before constriction, elongation during constriction, average constriction rate, N WT: 406, MreB*: 176

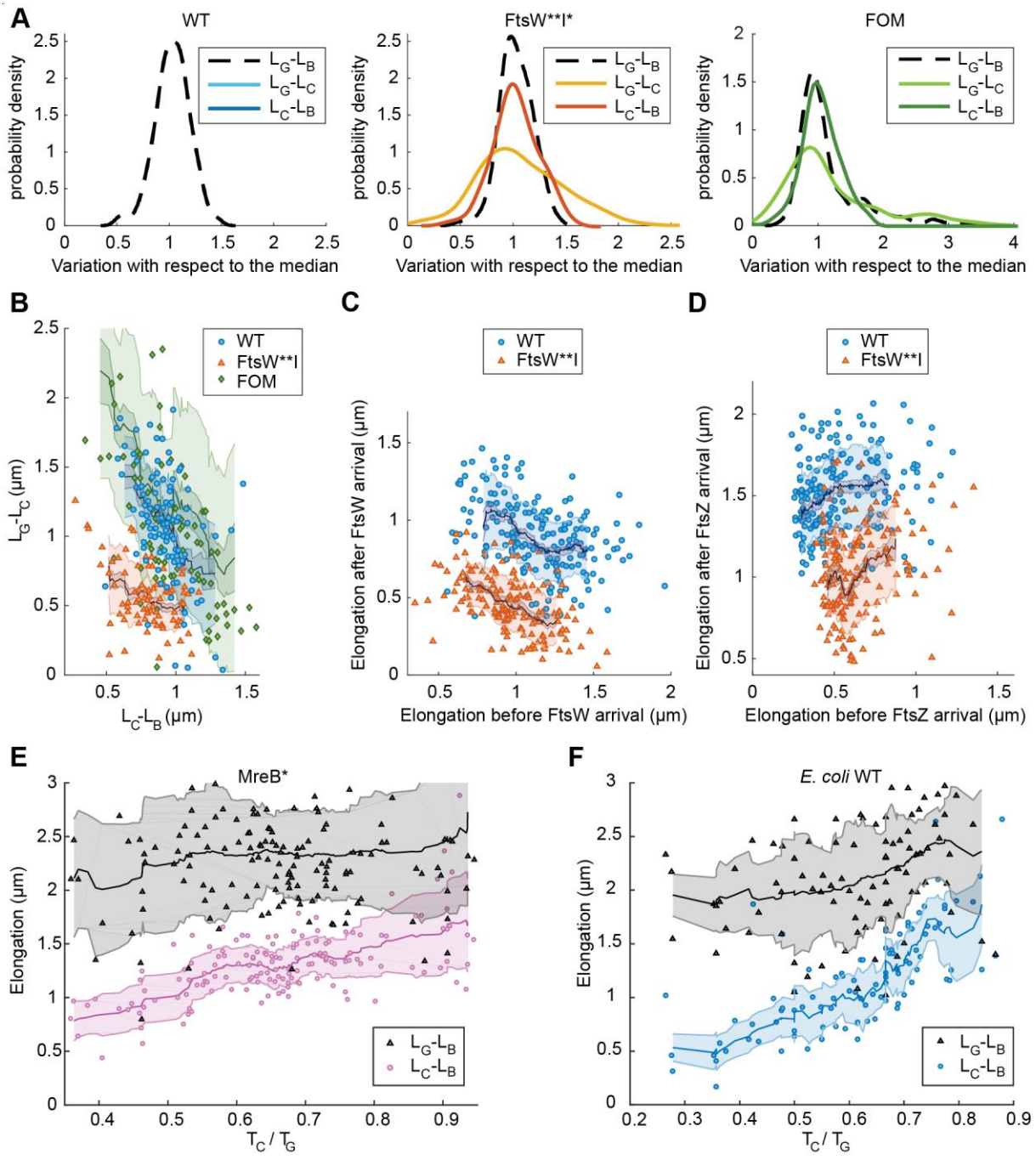

Figure S3. Constriction rate drives compensation between LG-LC and LC-LB, Related to Figure 3. **(A)** Variance in total elongation is smaller than the sum of the variance in elongation before and during constriction. Distribution of the measured elongation divided by median elongation. Onset defined by FtsW arrival. The variance of the sum of independent normal random variable *a* and *b* is equal to the sum of the variance: $\sigma_{a+b}^2 = \sigma_a^2 + \sigma_b^2$ where a and b are the elongation before and during constriction respectively. $\sigma_a^2 + \sigma_b^2$ is 0.144 μm² for the WT, 0.080 μm² for FtsW**I* and 1.26 μm² for FOM, which is significantly higher than σ_{a+b}^2 measured from the final total elongation distribution, which is 0.101 μm² for WT, 0.045 μm² for FtsW**I* and 1.04 μm² for FOM. (**B**) Scatterplot showing the elongation during constriction versus the elongation before constriction. Spearman correlation coefficients are: WT:r= -0.44, FtsW**I*: r=-0.32, FOM:r= -0.52, (**C**) Scatterplot of elongation during constriction versus before

constriction onset. Spearman correlation: WT: r = -0.44, p-value<0.005, FtsW**I*: r=-0.49, p-value<0.005 (**D**) Scatterplot of elongation after versus before FtsZ arrival. Spearman correlation: WT: Rho=0.20, p<0.005, Mut: r=0.26, p-value<0.005. (**E**). Total elongation (gray) and elongation before constriction (color) for individual MreB* mutant cells, as a function of normalized onset time (T_C/T_G). (**F**) Total elongation (gray) and elongation before constriction (color) for individual *E. coli* cells, as a function of normalized onset time (T_C/T_G). . Dark lines in (**B-F)** represent the 20 cells moving average; the shaded zones represent the moving standard deviation. Extreme outliers, deviating by more than two standard deviations have been omitted for the calculation of the moving average.

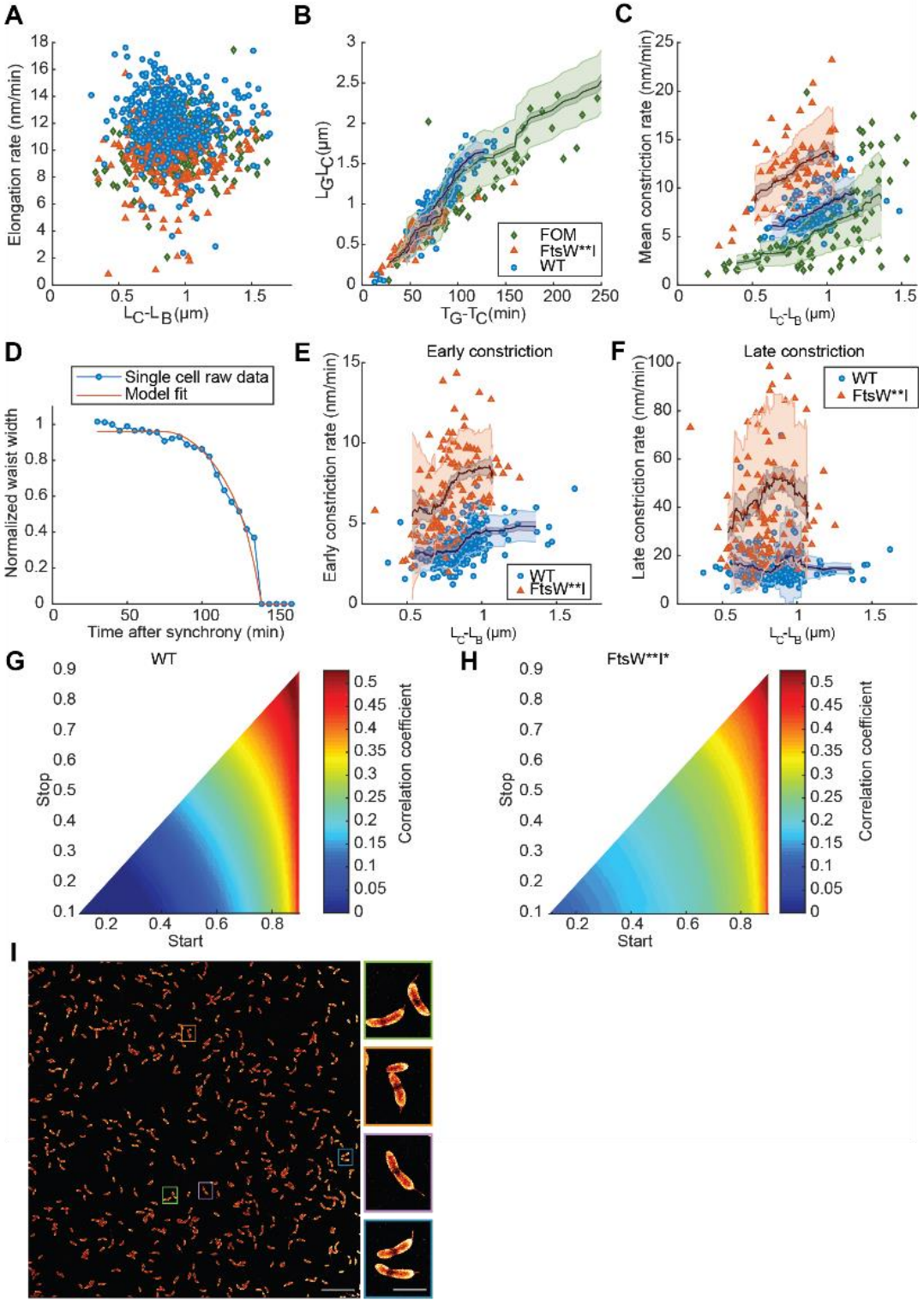
A
Elongation rate (nm/min)
L_C-L_B (μm)
B
L_G-L_C (μm)
T_G-T_C (min)
FOM
FtsW**I
WT
C
Mean constriction rate (nm/min)
L_C-L_B (μm)
D
Single cell raw data
Model fit
Normalized waist width
Time after synchrony (min)
E
Early constriction
Early constriction rate (nm/min)
WT
FtsW**I
L_C-L_B (μm)
F
Late constriction
Late constriction rate (nm/min)
WT
FtsW**I
L_C-L_B (μm)
G
WT
Stop
Start
Correlation coefficient
H
FtsW**I*
Stop
Start
Correlation coefficient
I

Figure S4. Constriction rate shows influence of elongation before constriction decreases throughout constriction, Related to Figure 4.

(**A**) Elongation rate during constriction is not responsible for compensation: Overall elongation rate during constriction versus elongation rate before constriction. Constriction onset is defined by visible constriction. N and Spearman's correlation coefficient: WT: N = 408, r = -0.11, p-value = 0.026, FtsW**I*: N = 358, r = -0.023, p-value = 0.67, FOM: N = 215, r = 0.30, p-value = $7x10^{-6}$. (**B**) Elongation during constriction versus the duration of constriction. Spearman correlation coefficients: WT: r = 0.90, FtsW**I*: r = 0.85, FOM: r = 0.94. N: WT: 96, FtsW**I*: 80, FOM: 102. (**C**) Relative duration of constriction ((TG-TC)/TG) versus elongation before constriction. Spearman Correlation coefficients: WT: r = 0.49 p-value<0.005, FtsW**I*: r = 0.46, p-value<0.005. N: WT: 96, FtsW**I*: 80, FOM: 102. (**D**) Example of a single cell normalized waist width versus time, fit with the empirical constriction model. (**E**) Early constriction rate, (supplemental note 2), in function of elongation before constriction. Early constriction rate is defined as the having a normalized waist width between 0.9 and 0.6. (**F**) Late constriction rate as a function of elongation before constriction. Late constriction rate is defined as the difference of diameter over the duration of the constriction, during late stage constriction from a normalized waist width of 60% to 30%. (**F**) WT: r = 0.11, p-value=0.13, FtsW**I*: r = 0.20, p-value=0.03. (**G**) Heatmap of correlation coefficient between elongation before constriction and constriction rate, as a function of over which portion of constriction the constriction rate is calculated. As in (**E**) and (**F**), the correlation between elongation before constriction and constriction rate was calculated. This was repeated for the constriction rate during various sub-periods of the constriction process, defined by the normalized waist width at the "start" and "stop" of the sub-period. See also Transparent Methods, Empirical constriction model. (**H**) Same as (**G**), but for FtsW**I*. Dark lines in (**B, C, E and** F) represent the 20 cells moving average; the shaded zones represent the moving standard deviation. Extreme outliers, deviating by more than two standard deviations have been omitted for the calculation of the moving average (**I**) STORM image of fixed C. crescentus cells stained with fluorescent wheat germ agglutinin, Right panels: Magnified views of the bacteria colors correspond to the area selected on the left panel. We used WGA-Alexa647 conjugated dye to stain C. crescentus cell wall. Scale bars 10 µm (Left panel), and 1 µm (Right panels).

TRANSPARENT METHODS

KEY RESOURCE TABLE

REAGENT or RESOURCE	SOURCE	IDENTIFIER
Experimental Models: Organisms/Strains		
NA1000, synchronizable derivative of wild-type CB15	(Evinger and Agabian, 1977)	CB15N
CB15N *ftsW(F145L,A246T); ftsI(I45V)*	(Modell et al., 2014)	ML2159
CB15N *Pxyl::ftsZ-GFP Pvan::MTS2-mCherry (GmR/KmR)*	This study	CB15NVL1
ML2159 *Pxyl::ftsZ-GFP Pvan::MTS2-mCherry (GmR/KmR)*	This study	CB15NVL2
CB15N *Pxyl::ftsW-GFP Pvan::MTS2-mCherry (GmR/KmR)*	This study	CB15NVL3
ML2159 *Pxyl::ftsW**-GFP Pvan::MTS2-mCherry (GmR/KmR)*	This study	CB15NVL4
CB15N *MreB(Q26P)*	(Aaron *et al.*, 2007)	CJW1715
CJW1715 *Pxyl::ftsZ-GFP Pvan::MTS2-mCherry (GmR/KmR)*	This study	CB15NVL5
K-12 MG1655 P_{lac}*::ftsZ-GFP* P_{BAD}*::MTS2-mCherry (ApR/CmR)*	This study	MG1655VL1
Oligonucleotides		
5'-AACTTGGTACCTCTAGAGGAAGATCTTTCATCGAGGAG-3'	This study	MTS2_KpnI-F
5'-AACTTGAATTC AAGCTTCTAGGATCCACCGCCG-3'	This study	MTS2_EcoRI-R
5'-CTCGAGCTCCGATGGCCTCCAACGCG-3'	This study	oEG035
5'-GTTCGAATTCTCTCAGGCGTCCGCGCGACC-3'	This study	oEG036
5'-AACTTGGTACCTCTAGAGGAAGATCTTTCATCGAGGAG-3'	This study	MTS2_KpnI-F
Plasmids		
Pxyl::VENN-2 FtsW (KmR)	(Goley et al., 2011)	pEG105
*Pxyl::VENN-2 FtsW** (KmR)*	This study	pEG1224
Pxyl:: GFPN-2*(KmR)*	(Thanbichler et al., 2007)	pXGFPN-2
Pxyl:: GFPC-2*(KmR)*	(Thanbichler et al., 2007)	pXGFPC-2
Pxyl::VENN-2(KmR)	(Thanbichler et al., 2007)	PXVENN-2
E. coli MTS2 fused to GFP pBAD33 derived plasmid *Para-GFP::EcMTS::EcMTS (CmR)*	(Szeto et al., 2003)	pSLR92
Pvan:: (KmR)	(Thanbichler et al., 2007)	pVCHYC-4

Pxyl::ftsZ-dendra2 (KmR) used to create pVL1	(Holden et al., 2014)	pX-Ftsz-Dendra2
Pxyl::ftsZ-GFP (KmR)	This study	pVL1
Pvan::MTS2-mCherry(GmR)	This study	pVL2
*Pxyl::GFPN-2 FtsW** (KmR)*	This study	pEG1308
Pxyl::VENN-2 FtsW (KmR)	(Goley et al., 2011)	pEG105
*Pxyl::VENN-2 FtsW** (KmR)*	This study	pEG1224
used to create pEG1305,pEG1308 (KmR)	This study	pXGFPN-2
Software and Algorithms		
sDaDa	This study	See Transparent methods and 10.5281/zenodo.1173751
Celltool	(Pincus and Theriot, 2007)	http://zplab.wustl.edu/celltool/
ImageJ	(Schneider et al., 2012)	https://imagej.nih.gov/ij/
MicrobeTracker	(Sliusarenko et al., 2011)	http://microbetracker.org/
MATLAB	The MathWorks, Natick, MA	https://ch.mathworks.com/products/matlab.html
Original data	This study	10.5281/zenodo.1248441 and 10.5281/zenodo.1241005

CONTACT FOR REAGENT AND RESOURCE SHARING

Further information and requests for resources and reagents should be directed to and will be fulfilled by the Lead Contact, Suliana Manley (suliana.manley@epfl.ch).

EXPERIMENTAL MODEL AND SUBJECT DETAILS

Bacterial strains and growth conditions

Strains and plasmids

The strains, plasmids, oligonucleotides, restriction sites and modes of constructions used for this study are summarized in Table S1. The WT and mutant strains were electroporated with the P_{van} mCherry-MTS2

plasmid to yield the P_{van} mCherry-MTS2 strain. These strains were then electroporated with the P_{xyl} FtsZ-GFP, P_{xyl} FtsW-GFP or P_{xyl} FtsW**-GFP plasmid to yield the respective dual color strains.

Growth conditions

Liquid *C. crescentus* cultures were grown overnight at 28°C with 15 mL of M2G minimal media under mechanical agitation (180 rpm). Each specific inducer for every different condition is described below. Fosfomycin perturbation was achieved with a subminimal inhibitory concentration of 12.5 µg/ml added one hour prior synchronization. To induce the expression of mCherry-MTS2 from the P_{van} promoter, 0.5 mM of vanillate was added to the culture before overnight growth. For the expression of FtsW-eGFP, xylose was added to reach a final concentration of 0.3 % (mass per volume) 2 hours before synchrony as optimized previously (Goley et al., 2011). P_{xyl} FtsZ-eGFP was induced overnight at 0.003 % xylose in M2G as optimized in a previous study (Holden et al., 2014).

Liquid *E. coli* cultures were grown overnight at 37°C in M9 medium under mechanical agitation (180rpm). mCherry-MTS2 was induced from the P_{BAD} promoter by adding 0.01% (m/V) arabinose during overnight growth. FtsZ-GFP was induced from the P_{lac} promoter using 20 µM Isopropyl β-D-1-thiogalactopyranoside (IPTG) for 2 hr prior to the experiment.

METHOD DETAILS

Sample preparation

C. crescentus cells were synchronized at 4°C by Percoll density gradient (Schrader and Shapiro, 2015) when they reached mid-exponential phase (OD_{660}=0.3-0.5).*E. coli* cells were not synchronized before the experiment, instead cell birth was identified from the time-lapse images. A silicone gasket (Grace Biolabs, 103280) was placed on a rectangular cover slide, and filled with 1% M2G agarose (Ultra PureTM Agarose, Sigma) containing fosfomycin, xylose and vanillate at the appropriate concentrations when needed. Vanillate was present at 0.5 mM in all experiments with *C, crescentus*, xylose was present at 0.003% for induction of FtsZ-eGFP, but absent for the FtsW-eGFP experiments. Fosfomycin was added to a final concentration of 10 µg/ml for drug perturbation experiments. For the *E. coli* experiments, 0.01% Arabinose was present in the M9-agarose pad. A cover slide was placed on top of the silicone gasket before

solidification of the agarose to achieve a flat agarose pad. After 5 min, the top cover slide was removed, and a 1 µL drop of a synchronized cells suspension was placed on the pad. A small piece of agarose (~1 mm) was cut out on two opposing sides to ensure aerobic conditions during imaging. After absorption of the droplet, the pad was sealed with a plasma-cleaned #1.5 round coverslip with a diameter of 25 mm.

Image acquisition

Microscope set up

SIM microscopy was performed on the 3D NSIM Nikon microscope, with a CFI Apochromat TIRF objective (100 x, NA 1.49, Nikon). The microscope was equipped with 400 mW, 561 nm and 480mW, 488 nm lasers (Coherent Sapphire) and a back-illuminated EMCCD camera (iXon 3, Andor Technology) with a 512x512 pixel CCD sensor.

Acquisition settings

Dual color imaging of the cells was performed at 28°C using the 488 nm and 561 nm lasers for the divisome protein-eGFP channel and the mCherry-MTS2 channel respectively. The camera was operated with a readout speed of 1 MHz and a dynamic range of 16 bit to have the maximum pixel readout speed at the highest dynamic range. The preamplifier gain and the electron multiplication gain were set to 1 and 200 respectively to maximize the signal to noise at the chosen dynamic range. All raw SIM images were acquired with a camera acquisition time of 200 ms and 100 ms (5 fps and 10 fps) for the 561 and 488 channels. The laser power for both channels was 4 W/cm2. These settings yielded a good balance between image quality and photo-bleaching.

All the raw images were acquired in 3D SIM image mode to ensure the highest signal to noise ratio and lateral resolution. Fifteen images were captured of each 30.7×30.7 µm field of view, five phase-shifted images per angle at each of three interference pattern angles. A full raw dual color image stack was acquired in 17s.

Live-cell fluorescence microscopy over the cell cycle was achieved by performing time-lapse imaging. 3D SIM snapshots were captured at 5 min or 10 min (for fosfomycin-treated cells) time intervals to follow dynamics while minimizing photo-bleaching of the sample during the image acquisition. Multiple fields of

view were imaged sequentially at each time point, allowing following up to 200 cells per experiment. Super-resolved SIM images were reconstructed by the Nikon NIS-Elements software.

Bleach correction

For visualization in Figure 1A and S1C, the images were bleach corrected based on the whole field of view, using the Bleach Correction function in ImageJ, using the "Simple Ratio" algorithm, for which the approximate background value was determined manually. Bleach correction was not performed for the analysis.

QUANTIFICATION AND STATISTICAL ANALYSIS

Analysis of cell shape dynamics

The super-resolved SIM images were processed via a custom-made software package called sDADA (Shape Dynamics Automated Data Analysis). sDADA generates scatter plots, histograms and violin plots in order to study key parameters controlling the cell size and homeostasis, such as: elongation rate, constriction duration, length at birth, onset, onset time. sDADA extracts these parameters from the analysis of the cell shape dynamics thanks to semi-interactive modules for image segmentation, edge detection, cell filtering, cell tracking and statistical analysis (See Detailed image analysis workflow). The MATLAB-based software package is available together with its documentation upon request. For the *E. coli* data, the septum is much more vertical than in *C. crescentus*, therefore it is no longer possible to robustly measure the early and late constriction rates with sDaDa, moreover, these cell could not be synchronized. For these data (Figure S3F), we manually identified cell birth, division onset and division times and lengths.

Parameter definition

We assumed as time zero (T_0) the time at which the suspension of synchronized bacteria is added to the agarose pad. This occurred approximately 20-40 minutes before starting time-lapse SIM acquisition. For *E. coli* data, T_0 was the time of first frame after the mother cell divided. T_C, T_Z, and T_W refer to the constriction onset time measured with different approaches. T_Z is the time of the FtsZ assembly, which we assumed to occur when the fluorescence intensity of FtsZ-eGFP at mid-cell was three times higher than elsewhere. T_W

is the FtsW arrival time measured as the moment at which the FtsW signal appeared stable at midcell (Figure S1C).

T_C is defined as the time at which the constriction invagination depth is equal to a predetermined normalized waist width threshold. To find the optimal threshold, we tested different thresholds in the reasonable range from 80% up to 99% of the maximum diameter, with step sizes of 1 %. Since FtsW arrival time is an alternative readout of the constriction start the Tc values computed from the waist diameter versus time should strongly and robustly correlate with the Tw values. For each threshold, we computed the Pearson's correlation coefficient for the scatter plot of the Tc values versus the Tw values of all the cells. We found that a threshold of 92% had the best correlation coefficient and minimal least square error for Tc versus Tw.

Generation time (T_G) and final length (L_G) are the time and the length at which the cell divide. Constriction duration τ is the difference between T_G and T_C, or when specified, T_W. The length at birth, L_B and the elongation rate k are extracted from the exponential fitting of the elongation: $\boldsymbol{L(t) = L_B \cdot e^{kt}}$.The length at the constriction onset, L_C, L_Z or L_W, were measured as the lengths at T_C, T_Z and T_W respectively. The total elongation is the difference between L_G and L_B. Elongation before constriction and during constriction are defined respectively as the difference between L_G and L_C, and between L_C and L_B. When specified, L_W can be used instead of L_C.

Statistical tests

For each parameter defined in the section above, the statistical significance of observed differences between strains or conditions was tested. We compared the means of the repeats using Mood's median test. The correlation between variables was analyzed using Pearson's correlation coefficient in the presence of a linear trend or the Spearman's correlation coefficient for non-linear relationship. The experiments were performed in two independent replicates per condition with a minimum of 100 cells analyzed per replicate, and 200 minimum per condition.

DETAILED IMAGE ANALYSIS WORKFLOW.

Cell shape dynamics and fluorescence measurement

A robust semi-automated pipeline was developed to identify, track and measure shape parameters (length, width, waist width) of hundreds of cells imaged in time lapse movies over the all cell cycle. Also distributions of the variables and correlations between variables were analyzed using this pipeline.

Drift correction

To simplify the tracking of cells over time, the time-lapse videos were drift-corrected using the Fiji plugin "Descriptor based registration (2d/3d + t)" (Preibisch et al., 2010). The dual-color experiment, registration of both channels was performed based on the drift observed in the red-channel (561nm).

sDaDa: a software package for supervised segmentation and measurement of bacterial images

The quantitative image analysis of the cell shape dynamics and of their fluorescent signals was performed with our custom-made software package called sDaDa (Shape Dynamics Automated Data Analysis). sDaDa is an open source MATLAB-based program for time-lapse dual color images of bacteria (FtsZ-GFP, FtsW-GFP (green channel) and mCherry-MTS2 (Szeto et al., 2003) (red channel)).

The program takes as input the time-lapse images stack (each superresolved image with a size of 1024 pixel x 1024 pixel; 30 nm /pixel), the camera parameter (i.e. pixel size) and a set of experimental parameters (i.e. starting time, time interval between two consecutive frames, the field of view (FOV)). The program outputs a data structure containing all the measurements of each cell at each frame and a set of figures with the results of the measurements.

The description of the main features of the sDaDa program and of the general steps in a typical pipeline (Figure S1) are presented below.

The main pipeline stages of the software are (1) image segmentation and first edge detection guess, (2) cell tracking, (3) edge detection refinement and shape parameters measurement, (4) divisome ring identification (5) shape parameters correlation analysis and outputs display.

More specifically, the segmentation step (1) is based on two processes: the first is based on the Otsu's thresholding method (Otsu, 1979) to distinguish background pixels from foreground one; the second group together a set of pixels by seeing which pixels are connected to each other. The Otsu's method sets a proper threshold via maximizing the inter-class variance of the bi-modal histogram of the pixel

intensities (foreground pixels and background pixels). Connected pixels that have a signal value higher than the threshold are tagged with the same number and identify as part of a cell only if they form an area bigger than 0.5 µm2. We used two built-in MATLAB functions (graythreshold() and bwlabel()) for Otsu's image thresholding and to identify each individual cell.

A microbeTracker function named model2mesh.m defines the first cell contour guess starting from the edge detection performed with buit-in MATLAB functions bwperim()and bwtraceboundary()). The model2mesh function retours two semi-contours, corresponding to the 'left' and 'right' sides of the cell. From the two semi-contours, the bacteria poles (the two farthest apart points on the contour) and the centerline (the average of the two half contour parts) can be easily identified.

Within the segmentation stage, the cell shape search, control and refinement is done thanks to an interactive tool.The user has several tools inspired by the MicrobeTracker (Sliusarenko et al., 2011) approach to manipulate the region, such as removing parts, joining two regions, smoothing, expanding. The user can also choose to delete the current time point of the cell or to mark the cell as divided, after which it will no longer be followed.

In order to track the same bacteria in successive frames (step (2)), the program performs a search based on a spatial analysis. The area and the barycenter position belonging to a cell in one frame is compared with the spatial distribution of pixels belonging to the possible corresponding cell in the following frame. The two regions correspond to the same cell if the difference between these two spatial distributions is lower than a user-defined tolerance parameter. The tracking search stops when the cell divides or when one region does not pass the search criteria.
The FtsZ and FtsW divisome assembly time (T_W and T_Z) is determined by monitoring the intensity profile along the centerline length over the cell cycle (step (4)). T_W and T_Z are the moments at which FtsZ and FtsW fluorescence signals reach their maximum intensity at the midcell.

The segmented regions, containing a well-identified cell, can therefore enter the second stage (3) where the program extracts and accurately measures the shape parameters described below.
The diameter is measured by taking perpendicular slices of the bacteria image along its centerline length. Using the intensity profile along each slice, a histogram with two maxima corresponding to the cell edge

will define the diameter. The intersection of the histogram with a line parallel to the abscise axis at half maximum high, identify up to four abscises (two for each maximum). The diameter is the difference between the two furthest apart abscises. Repeating this procedure for each slice of the bacteria, the diameter profile as a function of the length could be achieved (Figure S2). The minimum between two maxima of the diameter as a function of the length will then define the measure and the position of the constriction site. As a consequence, the waist width will be easily defined: the ratio of the width of the constriction site and the maximum diameter along the cell. Lastly, the length is measured by calculating the arc length of the centerline.

The program examines the temporal evolution of the length and the waist width for all single cells detected in a time-lapse experiment. From these curves, it extracts the elongation rate, the length at birth (L_B) and the division time (T_G). The onset time T_C and the duration of the constriction are measured as explained in the Methods “Parameter definition” section.

The volume and the surface area of a cell are estimated based on the measured widths along the length of the bacterium. The width versus the length profile is first smoothed using a spline function, to filter out the noise that would inflate the surface area estimation. The bacterium is assumed symmetric along its central axis. Therefore, assuming cross-sections perpendicular to the axis are circular, the volume and surface area can be computed by treating the measured ‘segments’ of the bacterium as a series of conical frusta.

The last stage (5) provides a set of statistical tools to study the correlations between the parameters extracted and to measure their average and variance. The user can generate a scatter plot for each possible couple of parameters combination (e.g. the scatter plots in Figure 3). Moreover, the user can generate a violin plot for each parameter to inspect its statistical distribution over the entire population (e.g. the violin plots in Figure 2). To conclude the program computes the correlation coefficient of each couple of parameters.

Analysis of cell poles was performed using the Celltool software package ((Pincus and Theriot, 2007); http://zplab.wustl.edu/celltool/). Image-derived cell shapes were converted into parametric spline curves (Pincus and Theriot, 2007), and centerlines were fit to each cell shape (as described in (Sycuro et al.,

2010)), again using Celltool. Cell poles were defined as the position on the cell outline closest to the ends of the centerline, and the curvature at that position was calculated from the first and second derivatives of the parametric spline x(t), y(t): curvature = $(x'y'' - y'x'')/(x'^2 + y'^2)^{3/2}$, where prime and double-prime represent the first and second derivatives, respectively. The "pole regions" used for PCA shape analysis were defined as all points within distance *d* from each endpoint, where *d* was set to 5% of the total cell perimeter (so 20% of the cell boundary was counted as one pole or the other). Principle modes of pole-shape variation were computed with Celltool, as previously described (Pincus and Theriot, 2007).

ESTIMATION OF EXCESS PEPTIDOGLYCAN PRECURSOR. Related to equation 1.

The assumptions and derivation are based on the work of Harris and Theriot (Harris and Theriot, 2016)

Assumption 1: Peptidoglycan precursor (P) production is proportional to the cell volume (V).

$$\frac{dP}{dt} = \gamma V \tag{1}$$

With γ being the rate constant of P production per unit of V, we assume γ is constant over the cell cycle (it changes over larger timescales than the generation time). $[\gamma] = \frac{mol}{\mu m^3}$

Assumption 2: PG precursor consumption is proportional to the increase in cell surface area (A):

$$\frac{dP}{dt} = -\lambda \frac{dA}{dt} \tag{2}$$

With λ being the rate constant of P consumption per unit of A, we assume λ is constant over the cell cycle (it changes over larger timescales than the generation time). $[\lambda] = \frac{mol}{\mu m^2}$

The total rate of change in precursor is then:

$$\frac{dP}{dt} = \gamma V - \lambda \frac{dA}{dt} \tag{3}$$

The amount of PG precursors produced between cell birth and an arbitrary time in the cell cycle, t_x, is calculated as follows, using exponential Volume growth:

$$\Delta P = [P]_{t_0}^{t_x} = \int_0^{t_x} \gamma V_0 e^{\alpha t}\, dt - \lambda(A_c - A_0) = \frac{\gamma}{\alpha} V_0 (e^{\alpha t_x} - 1) - \lambda \Delta A = \frac{\gamma}{\alpha} \Delta V - \lambda \Delta A$$

$$\Delta P = \frac{\gamma}{\alpha}\Delta V - \lambda \Delta A \quad (4)$$

Alternatively:

$$\frac{\Delta P}{\lambda} = \frac{\gamma}{\alpha\lambda}\Delta V - \Delta A \quad (5)$$

With ΔP, ΔV and ΔA being the increase in P, V and A respectively. $\frac{\Delta P}{\lambda}$ is the excess precursor expressed as the surface area that could be built with it. $\frac{\gamma}{\alpha\lambda}$ Expresses how volume growth results in production capacity of surface area. To find its value, we can use a **third assumption:** over a cell cycle, between birth and division of a cell, the amount of precursor that is produced equals the amount that is used, or the net production of precursor is zero:

$$0 = \frac{\Delta P}{\lambda} = \frac{\gamma}{\alpha\lambda}\Delta V - \Delta A$$

$$\frac{\gamma}{\alpha\lambda} = \langle\frac{\Delta A}{\Delta V}\rangle_{cell\ cycle} \quad (6)$$

If we apply (6) to (5), we get:

$$A_{excess} = \frac{\Delta P}{\lambda} = \langle\frac{\Delta A}{\Delta V}\rangle_{cell\ cycle}\,\Delta V - \Delta A \quad (7)$$

At the onset of constriction, when $t = T_C$, this can be written as:

$$A_{excess}(T_C) = \langle\frac{\Delta A}{\Delta V}\rangle_{cell\ cycle}\,\Delta V(T_C) - \Delta A(T_C) \quad (8)$$

Note that $\frac{\Delta P}{\lambda} = A_{excess}$describes the excess precursor as the amount of surface area that could be built with it.

EMPIRICAL CONSTRICTION MODEL. RELATED TO FIGURE S4.

<u>Early and late constriction rate determination (Fig S4E, F):</u>

Early constriction rate is defined in nm/min as the *difference of diameter over the duration of constriction, during early stage of constriction from a* normalized waist width *of 90% to 60%)*:

- Early constriction rate(nm/min)=($D_{(w=0,9)}$ - $D_{(w=0,6)}$)/($t_{(w=0,6)}$-t $t_{(w=0,9)}$)

Late constriction rate is defined in nm/min as the *difference of diameter over the duration of constriction, during late stage of constriction from a* normalized waist width *of 60% to 30%:*

Late constriction rate(nm/min)=($D_{(w=0,6)}$ - $D_{(w=0,3)}$)/($t_{(w=0,3)}$-t $t_{(w=0,6)}$)

Diameter and time coordinates at waist 0.9, 0.6, 0.3 were determined using linear interpolation.

Instantaneous constriction rate determination (Fig S4G, H):

To access instantaneous constriction rate (Figure S4G, H), we used a previously defined empirical model(Coltharp et al., 2016):

$$\left({}^{D(t)}/_{D_0}\right)^{\alpha} = 1 - ({}^{t}/_{(T_G - T_C)})^{\alpha}$$

Where D(t) is the diameter of the constriction site in function of time, t, while D0 is the diameter at constriction onset, ${}^{D(t)}/_{D_0}$ is the normalized waist width. TC is the time at constriction onset, while TG is the time when constriction and the cell cycle finishes. TG-TC is the duration of constriction. α is a variable reflecting the change in constriction rate. For constant constriction rate α equals 1, for a constant buildup of the area of hemispherical poles, α equals 2. Average values for α were 1.4 for the WT and 1.5 FtsW**I, suggesting cell wall remodeling rate slows down in both strains.

DATA AND SOFTWARE AVAILABILITY

All data and software used to support the results of this manuscript are available from the Lead Contact upon reasonable request. Original data is available on Zenodo, DOI: 10.5281/zenodo.1248441 and 10.5281/zenodo.1241005. Software is available on Zenodo, DOI: 10.5281/zenodo.1173751 and on github: https://github.com/LEB-EPFL/sDaDa

SUPPLEMENTAL REFERENCES

Coltharp, C., Buss, J., Plumer, T.M., and Xiao, J. (2016). Defining the rate-limiting processes of bacterial cytokinesis. Proc. Natl. Acad. Sci. U. S. A. *113*, E1044-1053.

Evinger, M., and Agabian, N. (1977). Envelope-associated nucleoid from Caulobacter crescentus stalked and swarmer cells. J. Bacteriol. *132*, 294–301.

Goley, E.D., Yeh, Y.-C., Hong, S.-H., Fero, M.J., Abeliuk, E., McAdams, H.H., and Shapiro, L. (2011). Assembly of the Caulobacter cell division machine. Mol. Microbiol. *80*, 1680–1698.

Harris, L.K., and Theriot, J.A. (2016). Relative Rates of Surface and Volume Synthesis Set Bacterial Cell Size. Cell *165*, 1479–1492.

Holden, S.J., Pengo, T., Meibom, K.L., Fernandez, C.F., Collier, J., and Manley, S. (2014). High throughput 3D super-resolution microscopy reveals Caulobacter crescentus in vivo Z-ring organization. Proc. Natl. Acad. Sci. *111*, 4566–4571.

Modell, J.W., Kambara, T.K., Perchuk, B.S., and Laub, M.T. (2014). A DNA Damage-Induced, SOS-Independent Checkpoint Regulates Cell Division in Caulobacter crescentus. PLoS Biol. *12*.

Pincus, Z., and Theriot, J.A. (2007). Comparison of quantitative methods for cell-shape analysis. J. Microsc. *227*, 140–156.

Preibisch, S., Saalfeld, S., Schindelin, J., and Tomancak, P. (2010). Software for bead-based registration of selective plane illumination microscopy data. Nat. Methods *7*, 418–419.

Schneider, C.A., Rasband, W.S., and Eliceiri, K.W. (2012). NIH Image to ImageJ: 25 years of image analysis. Nat. Methods *9*, 671–675.

Schrader, J.M., and Shapiro, L. (2015). Synchronization of Caulobacter Crescentus for Investigation of the Bacterial Cell Cycle. JoVE J. Vis. Exp. e52633–e52633.

Sliusarenko, O., Heinritz, J., Emonet, T., and Jacobs-Wagner, C. (2011). High-throughput, subpixel precision analysis of bacterial morphogenesis and intracellular spatio-temporal dynamics. Mol. Microbiol. *80*, 612–627.

Sycuro, L.K., Pincus, Z., Gutierrez, K.D., Biboy, J., Stern, C.A., Vollmer, W., and Salama, N.R. (2010). Peptidoglycan crosslinking relaxation promotes Helicobacter pylori's helical shape and stomach colonization. Cell *141*, 822–833.

Szeto, T.H., Rowland, S.L., Habrukowich, C.L., and King, G.F. (2003). The MinD Membrane Targeting Sequence Is a Transplantable Lipid-binding Helix. J. Biol. Chem. *278*, 40050–40056.

Thanbichler, M., Iniesta, A.A., and Shapiro, L. (2007). A comprehensive set of plasmids for vanillate- and xylose-inducible gene expression in Caulobacter crescentus. Nucleic Acids Res. *35*, e137.

NOBUYUKI OTSU (1979). A Threshold Selection Method from Gray-Level Histograms. IEEE Trans. SYSTREMS MAN Cybern. *SMC-9,*.